Received: 23 February 2017 | Revised: 29 May 2017 | Accepted: 30 May 2017

DOI: 10.1002/cnm.2906

RESEARCH ARTICLE - FUNDAMENTAL

WILEY

Robust nondimensional estimators to assess the nasal airflow in health and disease

E. Sanmiguel-Rojas[1] | M. A. Burgos[2] | C. del Pino[1] | M. A. Sevilla-García[3] | F. Esteban-Ortega[3]

[1]Escuela de Ingenierías Industriales, Andalucía Tech, Universidad of Málaga, Málaga, 29071, Spain

[2]Departamento de Ingeniería Térmica y de Fluidos, Universidad Politécnica de Cartagena, Cartagena, Spain

[3]Departamento de Otorrinolaringología, Hospital Universitario Virgen del Rocío, Seville, Spain

Correspondence
Enrique Sanmiguel-Rojas, Campus de Teatinos, Edificio de Ingenierías, Málaga 29071, Spain.
Email: enrique.sanmiguel@uma.es

Abstract

There are significant variations of both human nose shapes and airflow patterns inside nasal cavities, so it is difficult to provide a comprehensive medical identification using a universal template for what otolaryngologists consider normal breathing at rest. In addition, airflow patterns present even more random characteristics in diseased nasal cavities. To give a medical assessment to differentiate the nasal cavities in health and disease, we propose 2 nondimensional estimators obtained from both medical images and computational fluid dynamics. The first mathematical estimator ϕ is a function of geometric features and potential asymmetries between nasal passages, while the second estimator R represents in fluid mechanics terms the total nasal resistance that corresponds to the atmosphere-choana pressure drop. These estimators only require global information such as nasal geometry and magnitudes of flow determined by simulations under laminar conditions. We find that these estimators take low and high values for healthy and diseased nasal cavities, respectively. Our study, based on 24 healthy and 25 diseased Caucasian subjects, reveals that there is an interval of values associated with healthy cavities that clusters in a small region of the plane $\phi - R$. Therefore, these estimators can be seen as a first approximation to provide nasal airflow data to the clinician in a noninvasive method, as the computed tomography scan that provides the required images is routinely obtained as a result of the preexisting naso-sinusal condition.

KEYWORDS

3D model, airway dynamics, computational fluid dynamics, healthy and diseased nasal cavities

1 | INTRODUCTION

Human nasal anatomy differs considerably from subject to subject. This diversity hinders the identification of a generic relationship between normal airflow patterns and ventilation mechanisms of the healthy population. Unfortunately, there is no general agreement on how to find universal parameters to detect not only normal nasal airflows but also to analyze breathing for medical diagnosis.[1-6] Additionally, even though specialists in ENT clinics can diagnose different nasal conditions causing obstruction, the perception of nasal flow varies widely among individuals. Therefore, the results of the same surgery may differ from person to person depending on several aspects of the patient, such as ethnicity or gender.

Computational fluid dynamics (CFD) is a very useful tool with which to assess nasal airways.[7] In a review of the literature, Leong et al[8] analyzed the implications of CFD studies that offer an excellent method of studying nasal airflow patterns and physiology. Also, the reader is recommended to consult the thorough review of CFD in the assessment of nasal airflow and the

analysis of CFD limitations provided by Quadrio et al.[9] More recent and novel CFD efforts of Kannan et al[10,11] have extensively validated and analyzed airflows under different conditions in the airways and the nasal/oral sections (including the effect of turbulence, vorticity, and bifurcations). Conversely, Garcia et al[12] reported that the relationship between nasal resistance and air space minimal cross-sectional area (mCSA) remains unclear. However, they did propose that nasal resistance could be described by the Bernoulli Obstruction Theory, where a good agreement between CFD simulations and theory was found. They suggested that airway constrictions were rarely an exclusive contributor to nasal resistance, which might explain the weak correlation between mCSA and subjective nasal patency. In any case, CFD is a modern alternative methodology and it has been widely used to describe in great detail the nasal airways. However, CFD models that require millions of degrees of freedom to accurately describe the geometry and to reduce the discretization errors need several days to simulate one simple case. Recently, Kannan et al[13] modeled a pulmonary airflow with a new quasi-3D wire approach, much faster than CFD but with errors around 15%. Validation of the CFD technique with in vitro experiments in a realistic nasal airway geometry have been also performed.[14,15] Nevertheless, concepts in nasal cavities such as "disease" and "health" can be difficult to define precisely, especially in cases of nasal disease such as inflammation, sinusitis, polyps, etc, and in particular for before and after medical/surgical treatment. Hence, the establishment of a basic rule for the detection of the nasal cavities in health and disease seems to be complex. Therefore, the design of a good computer-aided diagnosis tool is highly desirable, with which to help the training and professional practice in the field of rhinology. In general, CFD continues to play an important role in the clinic and clinical decision making.[16,17] This is the main motivation of our work: to provide novel nondimensional estimators to distinguish a nasal cavity in health or disease, based on the combination of computed tomography (CT) images and CFD results to support rhinologists' medical diagnoses.

Many researchers have been using CFD during decades to find common airflow patterns in the healthy population, but no success has been achieved yet. For instance, numerical simulations obtained from 24 healthy subjects found that the nasal resistance in a region 3 cm from the nostril ranged from 52.6% to 78.3% of the total nasal airway resistance.[18] Segal et al[3] also analyzed the airflow pattern during restful breathing in four nasal CFD models from healthy subjects, and important variations in the formation of swirling flows and the presence of different spatial flow distributions were found. Zhao and Jiang[6] quantified variations of nasal geometry and airflow patterns in a patient cohort of 22 healthy subjects using CFD simulations. These authors correlated nasal airflow with morphological variables. They concluded that there are significant variations in nasal airflow patterns and properties within the healthy population, so they could not find a basic parameter with which to group their nasal cavities. Other interesting numerical work was developed by Zhang et al[19] who pointed out that the differences of 30 adult nasal cavities led to different airflow distributions and strong variations of the main airstream passing through the common nasal meatus. Again, there was a lack of a common parameter to identify the nasal cavities in health. Finally, the nasal airflow patterns during restful breathing in 3 healthy male subjects from Caucasian, Chinese, and Indian ethnic groups using CFD techniques were studied by Zhu et al.[20] The main flow path was found in the middle meatus, the inferior common meatus, and the middle common meatus for the Caucasian, the Chinese, and the Indian models, respectively. However, the relationship between nasal airflow variations and nasal functions remains unclear, not only for people of the same race but also from different racial or ethnic groups. Currently, a tool is needed that can assess every individual's nasal airflow.

The CFD is also increasing the effectiveness of surgery of many nasal diseases. For example, the effects on the pressure and temperature of the resection of the medial surface in the inferior turbinate have been analyzed computationally, plus associated septal deviation and nasal resistance.[21-25] The CFD modeling of a septal deviation has been also compared to a normal healthy nose,[26,27] and a full diagnosis can be accomplished. Moreover, septal perforations can result in nasal obstruction, sensation of dryness, crusting, whistling, headache, etc. Grant et al[28] and Pless et al[29] are examples of pioneering CFD work on this topic. Impairment of nasal airflow and physiological evidence in nasal obstruction caused by inferior turbinate hypertrophy, was studied numerically by Lee et al.[30] The surgical treatment of chronic nasal breathing difficulties still implies a significant degree of subjective judgement on the part of the surgeon, so a medical diagnosis based on quantitative data before and after the surgery should help accordingly.[9] The CFD supports a more scientific basis for the rhinologist's diagnosis. In addition, standard recommendations of intranasal medication vary significantly depending on the nasal cavity in health or disease.[31] Thereby, our proposed estimators could be applied not only before and after the surgery to identify the level of improvement quantitatively but also to how the identification of health and disease relates to the characteristics of the delivery system used by patients. It is a complete study for every nasal cavity airflow taking in account each individual's variations as encountered in the daily clinic.

In summary, the objective of this work is to introduce 2 robust nondimensional estimators to complete the medical assessment of the nasal cavities' airflow. Thus, these estimators will be important to the design of future software for computer-aided diagnosis. In the following section, some computational details are given. The definitions of both estimators are then developed. Finally, a statistic study of the results after applying the estimators for both sets of healthy and diseased populations are presented.

2 | PATIENT COHORT, COMPUTATIONAL MESH, NUMERICAL METHODS, AND SIMULATIONS

The nasal models presented in this work were built from CT scans collected from the database of the University Hospital *Virgen del Rocío* in Seville (Spain). A sample size of 49 Caucasian adults was studied and scanned for the entire nasal passage, ranging in age from 19 to 78 years and consisting of 31 females and 18 males. Furthermore, 24 subjects presented healthy nasal cavities, while 25 subjects presented nasal diseases with significant anatomical abnormalities such as deviated septum and nasal polyps. These disorders have been confirmed through previous medical evaluations. The 120 cross-sectional CT images of 0.4- to 0.6-mm thickness, with a spatial resolution of 512×512 pixels were obtained at coronal, sagittal, and axial locations. These snapshots are static, so the dynamic behaviour inside the nasal cavity is out of scope of our computational work.[32]

The migration from medical data of CT scans to a computational domain of the nasal geometry requires different stages, see Figure 1A. We developed an in-house numerical algorithm using Matlab (The MathWorks, Inc, Natick, Massachusetts) to build the geometry of the nasal model from sequential cross-sectional data.[3] The algorithm was based on the open-source *Insight Segmentation and Registration Toolkit* software, which is an object-oriented software system for image processing, segmentation,

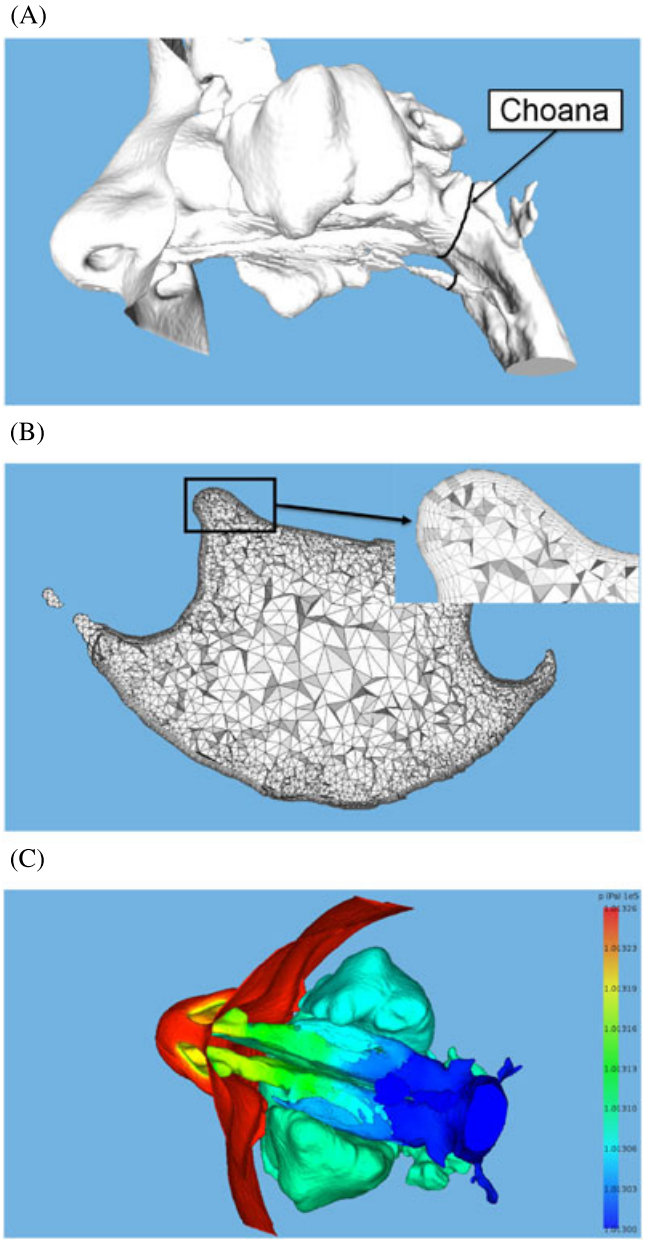

FIGURE 1 A, Geometry, B, mesh detail in the choana, and C, pressure contours for the inspiratory phase in Pa of one nasal cavity studied

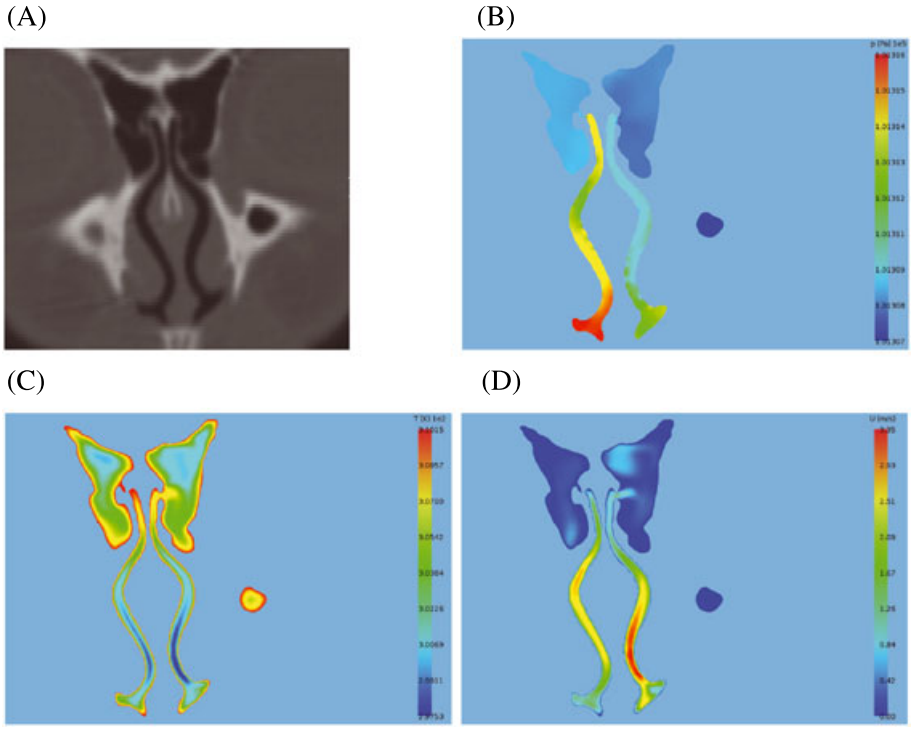

FIGURE 2 Transformation from medical data to a computational simulation. A, Computed tomography scan image and B, contours obtained from CFD of static pressure, C, temperature, and D, velocity modulus

and registration (http://www.itk.org/ItkSoftwareGuide.pdf). Specifically, the segmentation process has been performed using the *Watershed* filter. Afterward, the three-dimensional mesh of the nasal cavity was obtained using a file of commands formatted for the commercial mesh generation software Gambit (Fluent, Inc, Lebanon, New Hampshire). A mesh layer of prisms with variable thickness was built to simulate correctly the boundary layer of the air close to the walls, as shown in Figure 1B.

The laminar, steady-state,[33] and compressible flow simulations were discretized spatially with second-order accuracy of the Navier-Stokes equations by the finite volume software ANSYS Fluent. The pressure-velocity coupling was achieved by the pseudo-transient method to improve convergence. The inspiratory phase was performed by imposing a pressure drop between the atmosphere and the end of the computational domain, placed at the nasopharynx away from the choana. This kind of pressure boundary condition mimics the natural respiration process induced by lungs,[34] see Figure 1C. Furthermore, the computational domains include the external face allowing the flow to develop naturally towards the nostrils and letting a realistic effect of the inlet velocity profile dissipation after the nasal vestibule, see Figure 1A and 1C. The pressure drop remains constant to reach a global flow rate Q equal to or lower than 15 L/min to guarantee laminar flow during the inspiration phase.[34] The surface was modelled as rigid, no-slip, and at a constant static temperature of 37°C. The inflow static temperature was 21°C, and outflow boundary conditions for the temperature and velocity were imposed at the outlet.

The validation of numerical simulations was performed by using a grid convergence study that was performed following the procedure described in Burgos et al.[35] In particular, the flow rate Q, the static temperature T, and the velocity modulus U were calculated at strategic locations on 3 successively refined meshes. The absolute error between meshes for these quantities was less than 1%. For all numerical models, the calculations were performed with hybrid meshes ranging between 15 and 20 millions of cells (tetrahedra and prisms). For example, the mesh shown in Figure 1 has the following details: 20.45 millions of cells; 45.20 millions of faces; 1.57 millions of faces on the nasal surface. These values are at least 10 times greater than the numbers of cells used in most of the CFD simulations performed recently.[9] Finally, the example of the transformation from CT images to computational results of one random subject is depicted in Figure 2, where we show the original image (Figure 2A), contours of static pressure in Pa$\times 10^5$ (Figure 2B), temperature in K (Figure 2C), and velocity modulus in m/s (Figure 2D).

3 | DEFINITION OF THE NEW MATHEMATICAL ESTIMATORS

After analysing 49 healthy and diseased human nasal cavities, we found several distinguishing characteristics between both sets. Such characteristics are mainly related to geometric asymmetries and global fluid properties computed by numerical simulations.

Our observations lead towards 2 dimensionless mathematical estimators. It is worth noting that these mathematical estimators only need CT or MRI images and numerical simulations. Therefore, the information from a preliminary medical diagnosis is not necessary.

The first mathematical estimator ϕ takes into account a large subset of symptoms that are identified by the specialists in the ENT clinics as each patient presents. Thereby, ϕ has been mathematically defined to characterize the presence of airflow variations between nasal cavities, asymmetries in their morphologies, as well as nasal obstructions. These abnormalities appear frequently in diseased nasal cavities. Thus, ϕ is defined as,

$$\phi = \frac{1 + \left(\frac{A_R + A_L}{2A_C} - 1\right)^2}{(1 - \varepsilon p)\, q\eta + \varepsilon p}, \tag{1}$$

where

A_R is the area of the right nostril;
A_L is the area of the left nostril;
A_C is a mean nostril area. For the subjects studied in this work, it is found that $A_C = 107mm^2$. This value belongs to the range given by Lang[36];
$p = A_{mi}/A_{ma}$ is the minor-to-major nostril area ratio;
$q = Q_{mi}/Q_{ma}$ is the minor-to-major flow rate ratio between passages;
η is a variable set by default to one, except when there is a septal perforation, then it is set to zero;
ε is a (small) value that avoids the singularity of the mathematical estimator ϕ, so the denominator is never null. We impose $\varepsilon = 0.25$, and slight variations are found changing this parameter;

In general, the mathematical estimator ϕ will take low values (order of unity) for healthy nasal cavities and high values for diseased nasal cavities, especially with large asymmetries regarding geometric features or global fluid flow properties. In particular, the numerator in Equation 1 penalizes the nasal cavities with small and large nostrils compared with the mean value A_C that represents the most likely value. Thus, when the average of the nostril areas tends to A_C the numerator tends to one. The denominator penalizes the asymmetries in the flow rates between nasal passages. Figure 3 shows a typical example of the shape of the estimator versus the minor-to-major flow rate ratio q. Notice that when the flow rates into each passage are similar ($q \to 1$), the value of ϕ is minimum. However, when the asymmetry between flow rates grows ($q \to 0$), the estimator also increases. Most of the values of the minor-to-major flow rate ratio for the healthy cavities analysed in this research are approximately $q \simeq 0.7$. It is also noteworthy that the maximum of the estimator ϕ is reached when the nasal cavity has a septal perforation ($\eta = 0$) or a passage completely blocked ($q = 0$). To detect automatically the value of η directly from the numerical simulations, the flow rates are calculated at both nostrils and at the end of each passage. The variable η is equal to one in cases where the flow rate is the same at the nostril and at the end of the passage for each (right or left) passage, otherwise η is null.

The second dimensionless estimator, R, is defined as the bilateral or total nasal resistance, based on the unilateral resistance of the 2 passages given by the equation:

$$\frac{1}{R} = \frac{1}{R_R} + \frac{1}{R_L} \Rightarrow R = \left(\frac{1}{R_R} + \frac{1}{R_L}\right)^{-1}, \tag{2}$$

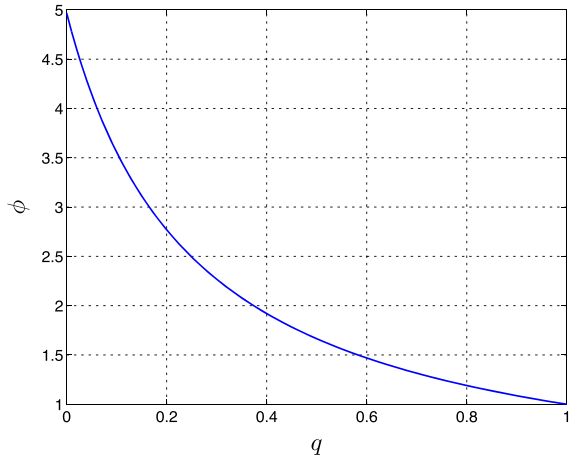

FIGURE 3 Estimator ϕ versus the minor-to-major flow rate ratio between nasal passages q. Nasal cavity without septal perforation ($\eta = 1$), A_R=118 mm^2 and A_L=95 mm^2 ($p \approx 0.8$), and $\varepsilon = 0.25$

where R_R and R_L are the unilateral resistances of the right and left passages, respectively. The dimensionless resistances proposed for each passage are

$$R_R = \frac{\Delta P/Q_R}{\frac{1}{2}\rho Q_R/A_R^2}, \tag{3}$$

$$R_L = \frac{\Delta P/Q_L}{\frac{1}{2}\rho Q_L/A_L^2}, \tag{4}$$

where ΔP is the pressure drop between the atmosphere and the choana, Q_R and Q_L are the flow rates into each nasal passage, A_R and A_L are the areas of each nostril, and $\rho \approx 1.2kg/m^3$ is the air density of the atmosphere. Both estimators R_R and R_L can be seen as Euler numbers applied to each nostril. Finally, note that the global flow rate into the nasal cavity can be expressed as

$$Q = Q_{mi} + Q_{ma} = Q_R + Q_L. \tag{5}$$

Although the estimation of ϕ and R could be derived from medical images (geometric features) and the use of rhinomanometry (flow rates and nasal resistance), numerical simulation is widely considered a more precise method. This precision is based on the drawbacks of using the raw clinical images without the postprocessed step in CFD to build the volume occupied by the fluid. Rhinomanometry presents 2 weaknesses: (1) It is intrusive due to the presence of several sensors that alter the breathing at rest, and (2) the resistance is measured with one nostril blocked, but not with the real contribution of each nostril while they work simultaneously.

Finally, it should be noted that a future challenge for CFD analysis is the requirement for large eddy simulations (LESs) to achieve the reliable objective patient-tailored diagnostic tool.[37] However, the authors believe that the robust estimators defined above that are based on global (not local or detailed) fluid properties using laminar simulations could be read as a first approximation for a good assessment, as will be presented below.

4 | RESULTS

4.1 | Application of the estimators to healthy and diseased nasal cavities

We apply the mathematical estimators for all the sample size, thus including the nasal cavities in health and disease. Specifically, 24 healthy subjects and 25 subjects with nasal diseases have been studied. Tables 1 and 2 show the results from such numerical simulations for healthy and diseased subjects, respectively. A brief description of the disease and some symptoms for each subject in the patient cohort is listed below:

D01: *Agenesis of the Vomer Bone*.
D02: *Adenocarcinoma of ethmoid sinus*.
D03: *Unilateral choanal atresia*. Asymptomatic with left mild rhinorrea.
D04: *Unilateral choanal atresia*. Asymptomatic with right mild rhinorrea.
D05: *Septal deviation*.
D06: *Inverted papilloma or Shneiderian papilloma*.
D07: *Septal perforation*.
D08: *Nasal polyps*. Postnasal drip together with anosmia, and halitosis.
D09: *Nasal polyps*. Postnasal drip together with anosmia, mouth breather, and snoring.
D10: *Allergic Rhinitis and hypertrophy of inferior turbinates with right inferior polypoid turbinate*.
D11: *Chronic sinusitis and Right antrochoanal polyps*.
D12: *Chronic sinusitis and septal deviation*.
D13: *Right antrochoanal polyp and mild septal deviation*.
D14: *Nasal polyps*. Postnasal drip together with anosmia.
D15: *Nasal polyps and septal perforation*.
D16: *Chronic sinusitis and septal deviation*. As subject D12, plus snoring, and mouth breather.
D17: *Nasal polyps*. Similar to D09.
D18: *Chronic sinusitis and septal deviation*. As subject D12 but with bilateral nasal blockage (Right > Left).
D19: *Chronic sinusitis and left maxilar mucocele*.
D20: *Septal deviation*. Right nasal blockage, nasal congestion and runny nose.

TABLE 1 Different parameters calculated in the inspiration phase by numerical simulation, for a set of 24 healthy (H#) nasal cavities

Subject	Q_R	Q_L	Q	A_R	A_L	ΔP	η
H01	8.00	6.70	14.70	111.00	94.00	22.00	1
H02	7.20	7.30	14.50	86.70	104.00	28.00	1
H03	7.70	6.80	14.50	103.40	95.00	28.00	1
H04	7.20	7.10	14.30	60.40	62.00	29.00	1
H05	4.00	10.78	14.78	122.20	129.10	17.00	1
H06	8.50	6.10	14.60	87.80	120.00	19.00	1
H07	8.40	6.10	14.50	93.30	93.00	42.00	1
H08	4.18	10.20	14.38	121.70	127.00	14.00	1
H09	5.50	8.40	13.90	60.30	71.00	19.00	1
H10	6.40	8.00	14.40	122.70	119.70	18.00	1
H11	7.00	7.80	14.80	128.00	124.00	10.00	1
H12	6.40	7.50	13.90	80.60	91.00	6.00	1
H13	7.70	6.40	14.10	99.80	83.30	12.00	1
H14	6.80	7.50	14.30	115.00	114.10	13.00	1
H15	8.20	6.30	14.50	161.70	178.80	17.00	1
H16	6.60	7.60	14.20	87.70	88.00	19.00	1
H17	4.70	9.70	14.40	121.50	111.80	20.00	1
H18	4.50	9.90	14.40	91.10	96.40	20.00	1
H19	5.50	8.80	14.30	103.00	86.80	17.00	1
H20	9.30	4.90	14.20	165.80	134.00	11.00	1
H21	7.70	6.50	14.20	115.20	115.50	16.00	1
H22	5.30	8.90	14.20	96.60	99.50	23.00	1
H23	6.50	7.60	14.10	97.00	108.20	15.00	1
H24	6.70	7.30	14.00	63.50	55.60	52.00	1

Flow rates (Q) in L/min, nostril areas (A) in mm^2, atmosphere-choana pressure drop (ΔP) in Pa, and the dimensionless septal perforation parameter η.

D21: *Nasal polyps and inferior hypertrophy of turbinates*.
D22: *Hypertrophy of inferior turbinates*.
D23: *Mild septal deviation*.
D24: *Septal deviation with concha bullosa (middle turbinate pneumatization)*.
D25: *Mild septal deviation with inferior bulky turbinates and concha bullosa (middle turbinate pneumatization)*.

We represent in Figure 4A the values of the estimator ϕ versus the estimator R, for both sets of healthy (circle) and diseased (cross) nasal cavities corresponding to the data included in Tables 1 and 2, respectively. A remarkable feature in the sample distribution is that, whereas circles get clustered to a small region in the plane $\phi - R$ close to the point $(R, \phi) = (10, 1)$, approximately, crosses are scattered into a large region. For the sake of the observation, we plot the same results in Figure 4B with axes in logarithmic scale. Therefore, the estimators tend to group the healthy cavities and to spread the diseased ones.

4.2 | Statistical analysis

In this section, we perform statistical analysis to identify 2 different regions of the plane $\phi - R$: regions A and B. It is found that these regions can be associated with healthy or diseased nasal cavities to different levels of probability.

Height and weight of a human population are common examples of variables that follow a normal (Gaussian) distribution. On the other hand, some examples of diseases with a normal distribution are ventilation distribution in human lungs with bronchoconstriction[38]; cholesterol levels[39]; age at onset in schizophrenia[40]; etc. In this research, we assume that the flow rates ratio, atmosphere-choana pressure drop, and nostril areas are continuous variables with normal distribution for both sets of healthy and diseased nasal cavities.

We show in Table 3 the mean and the standard deviation of both sets shown in Figure 4, to perform a statistical study of the probability of finding healthy or diseased cavities in different regions of the plane $\phi - R$.

TABLE 2 Different parameters calculated in the inspiration phase by numerical simulation, for a set of 25 diseased (D#) nasal cavities

Subject	Q_R	Q_L	Q	A_R	A_L	ΔP	η
D01	6.70	7.46	14.15	53.62	56.21	22.00	1
D02	0.00	15.00	15.00	183.51	159.70	79.00	1
D03	14.90	0.01	14.91	87.00	81.00	355.00	1
D04	1.60	13.20	14.80	118.00	95.00	112.00	1
D05	10.30	4.60	14.90	75.50	69.00	18.00	1
D06	0.00	14.80	14.80	123.00	142.00	751.00	1
D07	8.10	6.80	14.90	94.00	95.40	36.00	0
D08	4.10	10.80	14.90	147.50	136.80	10.00	1
D09	5.60	9.30	14.90	52.80	56.00	73.00	1
D10	4.40	10.10	14.50	81.30	82.30	17.00	1
D11	3.80	10.40	14.20	79.00	67.00	105.00	1
D12	10.10	4.80	14.90	202.00	144.00	12.00	1
D13	7.10	7.50	14.60	134.50	153.40	22.00	1
D14	4.50	9.50	14.00	57.60	85.00	24.00	1
D15	6.40	8.40	14.80	159.70	188.70	13.00	0
D16	13.60	0.60	14.20	118.40	156.00	507.00	1
D17	9.70	4.10	13.80	88.70	62.70	44.00	1
D18	4.45	9.90	14.35	128.70	114.10	11.00	1
D19	11.20	2.90	14.10	88.60	97.80	17.00	1
D20	2.80	11.40	14.20	96.70	88.00	60.00	1
D21	0.00	14.20	14.20	126.00	117.80	70.00	1
D22	5.50	8.70	14.20	155.00	122.00	209.00	1
D23	10.50	3.75	14.25	142.80	111.30	73.00	1
D24	12.20	1.40	13.60	86.80	137.20	22.00	1
D25	9.60	4.10	13.70	72.70	69.50	57.00	1

Flow rates (Q) in L/min, nostril areas (A) in mm^2, atmosphere-choana pressure drop (ΔP) in Pa, and the dimensionless septal perforation parameter η.

To apply the standard normal distribution, we define the standardized variables,

$$x_H = \frac{R - \bar{R}_H}{\sigma_R^H}, \quad y_H = \frac{\phi - \bar{\phi}_H}{\sigma_\phi^H}, \tag{6}$$

for the healthy cavities and,

$$x_D = \frac{R - \bar{R}_D}{\sigma_R^D}, \quad y_D = \frac{\phi - \bar{\phi}_D}{\sigma_\phi^D}, \tag{7}$$

for the diseased cavities. Note that these standardized variables have a mean value of zero and a standard deviation of one. The definitions for the different probabilities used in the calculations are as follows (see Figure 5 to distinguish regions A and B):

P_A^H is the probability that a healthy cavity falls inside region A.
P_B^H is the probability that a healthy cavity falls inside region B.
P_A^D is the probability that a diseased cavity falls inside region A.
P_B^D is the probability that a diseased cavity falls inside region B.
$\mathcal{P}_A^H$ is the probability that a cavity inside region A is healthy.
$\mathcal{P}_B^H$ is the probability that a cavity inside region B is healthy.
$\mathcal{P}_A^D$ is the probability that a cavity inside region A is diseased.
$\mathcal{P}_B^D$ is the probability that a cavity inside region B is diseased.

Notice that the previous definitions fulfill,

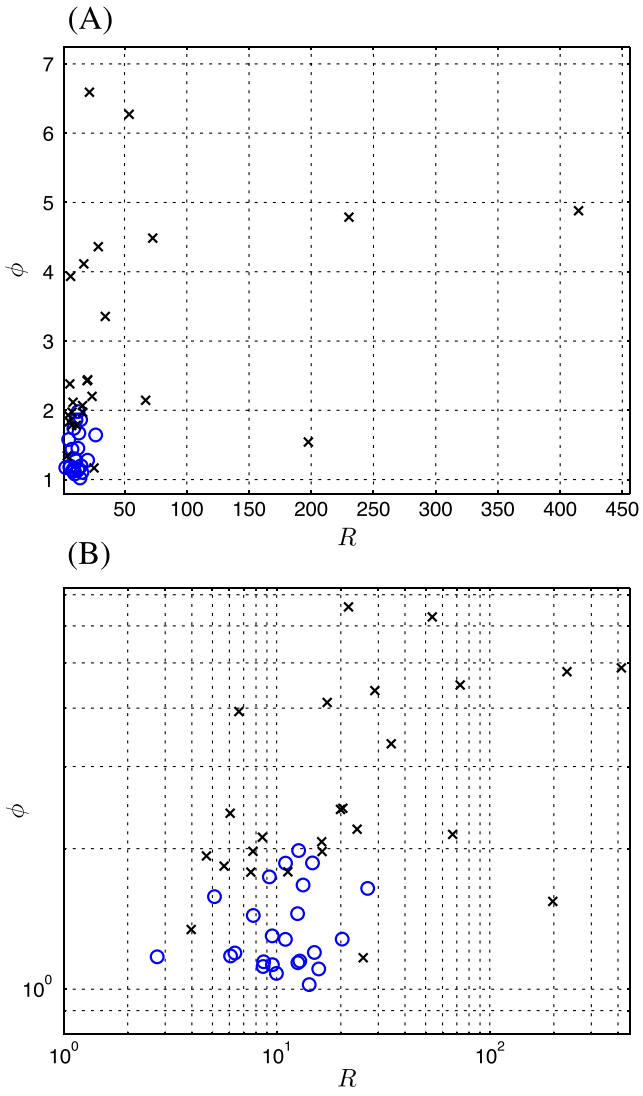

FIGURE 4 Plane $\phi - R$ in A, linear and B, logarithmic scales. Nasal cavities in health (circle) and disease (cross)

TABLE 3 Mean (overbar) and standard deviation (σ) of the values shown in Figure 4 corresponding to the nasal cavities in health H and disease D

$\bar{R}_H$	σ_R^H	$\bar{\phi}_H$	σ_ϕ^H	$\bar{R}_D$	σ_R^D	$\bar{\phi}_D$	σ_ϕ^D
11.52	4.94	1.36	0.28	52.92	92.22	2.97	1.50

$$\begin{aligned} P_A^H + P_B^H &= 1, \\ P_A^D + P_B^D &= 1, \\ \mathcal{P}_A^H + \mathcal{P}_A^D &= 1, \\ \mathcal{P}_B^H + \mathcal{P}_B^D &= 1. \end{aligned} \tag{8}$$

Furthermore, the probabilities $\mathcal{P}$ are related to P following the expressions,

$$\begin{aligned} \mathcal{P}_A^H &= \frac{P_A^H}{P_A^H + P_A^D}, \quad \mathcal{P}_A^D = \frac{P_A^D}{P_A^H + P_A^D}, \\ \mathcal{P}_B^H &= \frac{P_B^H}{P_B^H + P_B^D}, \quad \mathcal{P}_B^D = \frac{P_B^D}{P_B^H + P_B^D}. \end{aligned} \tag{9}$$

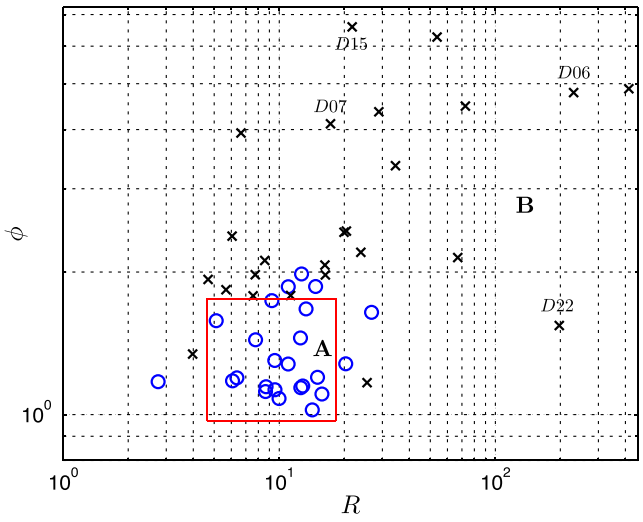

FIGURE 5 Plane $\boldsymbol{\phi - R}$ in logarithmic scale. Healthy cavity (circle) and diseased cavity (cross). Region A (red rectangle) corresponds to a probability $\mathcal{P}_A^H = 99\%$

The size of the region A (red rectangle) shown in Figure 5 was set for a probability $P_A^H = 70\%$. Below, it is demonstrated that this value is good enough to guarantee a probability greater than 95% to find inside region A one healthy cavity. Since the flow rate ratio and the atmosphere-choana pressure drop are independent variables, to fix the edges of the rectangle we solved the following expression,

$$P_A^H = 0.7 = [2P(x_H \leqslant a) - 1] \cdot \left[2P(y_H \leqslant a) - 1\right], \tag{10}$$

where $P(x_H \leqslant a)$ is the Gaussian probability that x_H is less or equal than the value to be found a. Taking into account that $P(x_H \leqslant a) = P(y_H \leqslant a) = P$, is obtained from Equation 10 is found that $P \approx 0.9183$. Finally, from a table of probabilities of the standard normal distribution for $P \approx 0.9183 \Rightarrow a \approx 1.39$. Therefore, the rectangle shown in Figure 5 corresponds to the region A in the plane $\phi - R$ defined as,

$$\begin{cases} -a \leqslant \frac{R-\bar{R}_H}{\sigma_R^H} \leqslant a, \\ -a \leqslant \frac{\phi-\bar{\phi}_H}{\sigma_\phi^H} \leqslant a. \end{cases} \tag{11}$$

To determine the probability P_A^D that a diseased cavity falls inside the region A, one has to solve the following expression,

$$\begin{aligned} P_A^D = &\left[P(x_D \leqslant \tfrac{R-\bar{R}_D}{\sigma_R^D})\Big|_{R=\bar{R}_H+a\sigma_R^H} - P(x_D \leqslant \tfrac{R-\bar{R}_D}{\sigma_R^D})\Big|_{R=\bar{R}_H-a\sigma_R^H}\right] \cdot \\ &\cdot \left[P(y_D \leqslant \tfrac{\phi-\bar{\phi}_D}{\sigma_\phi^D})\Big|_{\phi=\bar{\phi}_H+a\sigma_\phi^H} - P(y_D \leqslant \tfrac{\phi-\bar{\phi}_D}{\sigma_\phi^D})\Big|_{\phi=\bar{\phi}_H-a\sigma_\phi^H}\right] \approx 0.007 = 0.7\%. \end{aligned} \tag{12}$$

Therefore, the probability that a diseased nasal cavity falls inside the rectangle that forms region A is only 0.7%. Once we know the values, P_A^H and P_A^D, it is possible to compute other probabilities from Equations 8 and 9 yielding,

$$\begin{aligned} P_B^H &= 1 - P_A^H = 1 - 0.7 = 0.3 = 30\%, \\ P_B^D &= 1 - P_A^D = 1 - 0.007 = 0.993 = 99.30\%, \\ \mathcal{P}_A^H &= \frac{P_A^H}{P_A^H + P_A^D} = 0.9901 \approx 99\%, \\ \mathcal{P}_A^D &= 1 - \mathcal{P}_A^H = 0.0099 \approx 1\%, \\ \mathcal{P}_B^H &= \frac{P_B^H}{P_B^H + P_B^D} = 0.2320 = 23.20\%, \\ \mathcal{P}_B^D &= 1 - \mathcal{P}_B^H = 0.7680 = 76.80\%. \end{aligned}$$

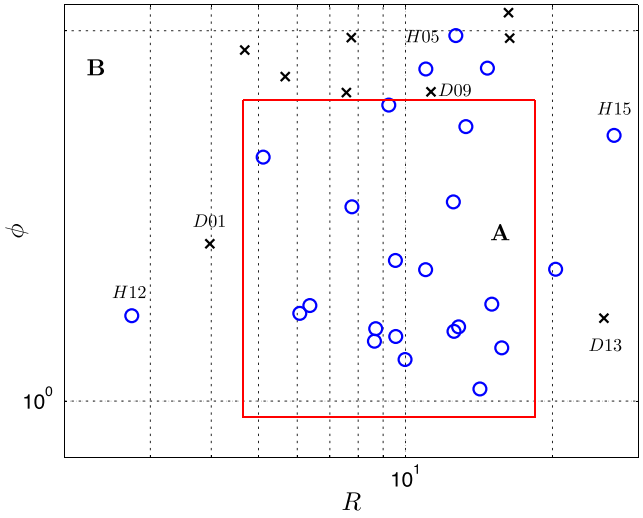

FIGURE 6 Zoom of region A from Figure 5

To summarize, the main conclusion we can draw is that the probability to find a healthy cavity inside region A is very high, namely, $\mathcal{P}_A^H = 99\%$. Furthermore, the probability to find a diseased cavity inside region A is very low, ie, $\mathcal{P}_A^D = 1\%$. In our study based on 49 subjects, it is noted that only healthy cavities fall inside region A (see Figure 5). It is also noteworthy that there is a high probability, $\mathcal{P}_B^D = 76.80\%$, to find a diseased cavity inside region B (outside region A).

To understand the relationship between the characteristics of the nasal cavity and its position in the plane (ϕ-R), some extreme values of the estimators for the nasal diseases have been marked in Figure 5. Specifically, the values $D07$ and $D15$ correspond to cavities with septal perforation. On the other hand, the value $D06$ has the right passage blocked with very large atmosphere-choana pressure drop (751 Pa). However, value $D22$ has again large pressure drop between the atmosphere and the choana (209 Pa). Therefore, both estimators tend to markedly recognize characteristics such as septal perforation, blocked passage or high pressure drop along the cavity, which are linked to different types of disease.

Figure 6 shows a zoom of the region A. Some values inside region B, but close to the border of region A, have been marked for both sets. In particular, for healthy cavities, value $H12$ falls on the left and corresponds to a healthy cavity, but with an unusually low pressure drop (6 Pa). $H05$ falls above but outside region A. However, this healthy cavity exhibits a moderate asymmetry in the passage flow rates. Finally, out of region A, and on the right, falls the healthy cavity $H15$ with very large nostrils. Thus, these three values are examples of healthy cavities that fall outside the region A, but with unusual characteristics such as low pressure drop, flow rate asymmetry, or large nostrils. Conversely, some diseased cavities with values very close to region A have been depicted in Figure 6. $D01$ falls on the left and close to the border of region A. This cavity has a relatively low pressure drop (22 Pa) for the diseased set, and the nostril areas are very small ($\approx$50 mm^2). $D09$ has nasal polyps and also falls near region A. This case has a relatively high value of pressure drop (75 Pa); however, the estimators are not able to identity it clearly as a diseased case. Finally, $D13$ falls on the right and moderately close to region A. This case also has a relatively low pressure drop (22 Pa) for a diseased cavity, but it has large nostril areas ($>$130 mm^2). Therefore, both healthy and diseased subjects can be found inside region B but near the border of region A (red rectangle). Consequently, special cases require the help of the otolaryngologist in order to attain a good medical diagnosis.

In summary, we can confirm that the cases that fall very close to the border of region A are difficult to be classified as healthy or diseased with these estimators. Therefore, special attention must be paid to the cases close to the border between region A and B. On the other hand, the values that fall inside region A, or far from it, belong to healthy or diseased sets, respectively. However, we have to take into account that these estimators are based only on geometrical characteristics or fluid magnitudes calculated by numerical simulations. A definitive diagnosis can only be made by otolaryngologists, with the goal of these mathematical estimators being to help them in their assessment.

5 | CONCLUSIONS

We introduce 2 dimensionless mathematical estimators on which to base computer-aided diagnosis of human nasal cavities in health and disease. The main objective is that a preliminary medical opinion is not essential because the estimators only

require information from medical images and numerical simulations. An in-house numerical algorithm using Matlab was developed to build the geometry of the nasal model from CT images. The nasal airflow was obtained by numerical simulation with the commercial software ANSYS Fluent under laminar and steady-state conditions. The first estimator ϕ is a function of potential asymmetries in geometric features and fluid flow magnitudes. The second estimator R represents the nondimensional atmosphere-choana pressure drop in both nostrils. These estimators were applied to a sample size of 49 Caucasian subjects, 24 being healthy and 25 presenting some nasal disorders. It is found that the healthy nasal cavities cluster to a small region in the plane $\phi - R$. Furthermore, a statistical study reveals that there is a 99% probability to find a cavity to be healthy if in this region. However, the patients with diseased nasal cavities present values of the estimators that show a high dispersion. Therefore, these novel estimators can be considered part of the assessment strategy to distinguish the nasal cavities in health and disease. This fact proves that the robust mathematical estimators presented in this work should lead to a solid identification in the future practice of personalised medicine.

Finally, more studies are required to further extend this work to a large sample of Caucasian population, thus including more variations in age, health status, or gender. Furthermore, these estimators should be applied to other ethnic groups to find regions corresponding to the nasal cavities in health and disease. This last study would help to check the similarities or differences between different ethnic groups in the plane $\phi - R$.

ACKNOWLEDGEMENTS

The authors acknowledge the access to the patient database of the University Hospital *Virgen del Rocío* of Seville (Spain). The authors would like to thank Dr Piers Treacher for his suggestions to improve the English style.

ORCID

E. Sanmiguel-Rojas http://orcid.org/0000-0003-0888-1984

REFERENCES

1. Broms P, Jonson B, Lamm CJ. A universal way to evaluate the curve in rhinomanometry. *Acta Oto-Laryngologica*. 1978;86:22-23.
2. Eccles R. Nasal airflow in health and disease. *Acta Oto-Laryngologica*. 2000;120(5):580-595.
3. Segal R, Kepler G, Kimbell J. Effects of differences in nasal anatomy on airflow distribution: a comparison of four individuals at rest. *Ann Biomed Eng*. 2008;36:1870-1882.
4. Doorly DJ, Taylor DJ, Schroter RC. Mechanics of airflow in the human nasal airways. *Respir Physiol & Neurobiol*. 2008;163:100-110.
5. Hill D, Binions R. Breath analysis for medical diagnosis. *Int J Smart Sens Int Syst*. 2012;5:401-440.
6. Zhao K, Jiang J. What is normal nasal airflow? A computational study of 22 healthy adults. *Int Forum Allergy Rhinology*. 2014;4:435-446.
7. Martonen T, Quan L, Zhang Z, Musante CJ. Flow simulation in the human upper respiratory tract. *Cell Biochem Biophys*. 2002;37(1):27-36.
8. Leong S, Chen X, Lee H, Wang D. A review of the implications of computational fluid dynamic studies on nasal airflow and physiology. *Rhinology*. 2010;48:139-145.
9. Quadrio M, Pipolo C, Corti S, Lenzi R, Messina F, Pesci C, Felisati G. Review of computational fluid dynamics in the assessment of nasal air flow and analysis of its limitations. *Eur Arch Oto-Rhino-Laryngology*. 2014;271(9):2349-2354.
10. Kannan R, Guo P, Przekwas A. Particle transport in the human respiratory tract: formulation of a nodal inverse distance weighted Eulerian-Lagrangian transport and implementation of the Wind-Kessel algorithm for an oral delivery. *Int J Numer Methods Biomed Eng*. 2016;32(6):e02746.
11. Kannan RR, Przekwas A, Singh N, Delvadia R, Tian G, Walenga R. Pharmaceutical aerosols deposition patterns from a dry powder inhaler: Euler lagrangian prediction and validation. *Med Eng Phys*. 2017;42:35-47.
12. Garcia G, Hariri BM, Patel RG, Rhee JS. The relationship between nasal resistance to airflow and the airspace minimal cross-sectional area. *J Biomech*. 2016;49:1670-1678.
13. Kannan R, Chen Z, Singh N, Przekwas A, Delvadia R, Tian G, Walenga R. A quasi-3d wire approach to model pulmonary airflow in human airways. *Int J Numer Methods Biomed Eng*. 2016. DOI: 10.1002/cnm.2838.
14. Croce C, Fodil R, Durand M, Sbirlea-Apiou G, Caillibotte G, Papon J, Blondeau J, Coste A, Isabey D, Louis B. In vitro experiments and numerical simulations of airflow in realistic nasal airway geometry. *Ann Biomed Eng*. 2006;34:997-1007.
15. Mylavarapu G, Murugappan S, Mihaescu M, Karla M, Khosla S, Gutmark K. Validation of computational fluid dynamics methodology used for human upper airway flow simulations. *J Biomech*. 2009;42:1553-1559.
16. Sznitman J, Steinman DA. Relevance and challenges of computational fluid dynamics in the biomedical sciences. *J Biomech*. 2016;49(11):2101.
17. Zhang J. Characteristic size research of human nasal cavity and the respiratory airflow CFD analysis. *J Biosci Med*. 2013;1:23-27.
18. Yu S, Liu Y, Sun X, Li S. Influence of nasal structure on the distribution of airflow in nasal cavity. *Rhinology*. 2008;46:137-143.
19. Zhang J, Liu Y, Sun X, Yu S, Yu C. Computational fluid dynamics simulations of respiratory airflow in human nasal cavity and its characteristic dimension study. *Acta Mech Sinica*. 2008;24(2):223-228.

20. Zhu JH, Lee HP, Lim KM, Lee SJ, Wang DY. Evaluation and comparison of nasal airway flow patterns among three subjects from Caucasian, Chinese and Indian ethnic groups using computational fluid dynamics simulation. *Respiratiry Physiol Neurobiol*. 2011;175(1):62-69.
21. Lindemann J, Keck T, Wiesmiller K, Rettinger G, Brambs H, Pless D. Numerical simulation of intranasal air flow and temperature after resection of the turbinates. *Rhinology*. 2005;43:24-28.
22. Wexler D, Segal R, Kimbell J. Aerodynamic effects of inferior turbinate reduction: Computational fluid dynamics simulation. *Arch Otolaryngology Head Neck Surg*. 2005;131:1102-1107.
23. Kimbell J, Frank D, Laud P, Garcia G, Rhee J. The relationship between nasal resistance to airflow and the airspace minimal cross-sectional area. *J Biomech*. 2013;46:2634-2643.
24. Garcia G, Rhee J, Senior B, Kimbell J. Septal deviation and nasal resistance: an investigation using virtual surgery and computational fluid dynamics. *Am J Rhinology Allergy*. 2010;24:46-53.
25. Ozlugedik S, Nakiboglu G, Sert C, Elhan A, Tonuk E, Akyar S, Tekdemir I. Numerical study of the aerodynamic effects of septoplasty and partial lateral turbinectomy. *Laryngoscope*. 2008;118:330-334.
26. Zhao K, Pribitkin E, Cowart B, Rosen D, Scherer P, Dalton P. Numerical modeling of nasal obstruction and endoscopic surgical intervention: outcome to airflow and olfaction. *Am J Rhinology*. 2006;20(3):308-316.
27. Chen X, Lee H, Hin Chong V, Wang D. Assessment of septal deviation effects on nasal air flow: a computational fluid dynamics model. *Laryngoscope*. 2009;119:1730-1736.
28. Grant O, Bailie N, Watterson J, Cole J, Gallagher G, Hanna B. Numerical model of a nasal septal perforation. *Stud Health Technol Inf*. 2004;107:1352-1356.
29. Pless D, Keck T, Wiesmiller K, Lamche R, Aschoff A, Lindemann J. Numerical simulation of airflow patterns and air temperature distribution during inspiration in a nose model with septal perforation. *Am J Rhinology*. 2004;18:357-362.
30. Lee H, Poh H, Chong F, Wang D. Changes of airflow pattern in inferior turbinate hypertrophy: a computational fluid dynamics model. *Am J Rhinology Allergy*. 2009;23(2):153-158.
31. Mygind N, Dahl R. Anatomy, physiology and function of the nasal cavities in health and disease. *Adv Drug Delivery Rev*. 1998;29:3-12.
32. Chouly F, Van Hirtum A, Lagrée P-Y, Pelorson X, Payan Y. Numerical and experimental study of expiratory flow in the case of major upper airway obstructions with fluid–structure interaction. *J Fluids Struct*. 2008;24:250-269.
33. Hörschler I, Schröder W, Meinke M. On the assumption of steadiness of nasal cavity flow. *J Biomech*. 2010;43:1081-1085.
34. Taylor D, Doorly D, Schroter R. Inflow boundary profile prescription for numerical simulation of nasal airflow. *J R Soc Interface*. 2010;7(44):515-527.
35. Burgos MA, Sanmiguel Rojas E, Martín Alcántara A, Hidalgo-Martínez M. Effects of the ambient temperature on the airflow across a Caucasian nasal cavity. *Int J Numer Methods Biomed Eng*. 2014;30:430-445.
36. Lang J. *Clinical Anatomy of the Nose, Nasal Cavity and Paranasal Sinuses*. New York: Thieme Medical Publishers, Inc.; 1989.
37. Kim S, Na Y, Kim JI, Chung SK. Patient specific cfd models of nasal airflow: overview of methods and challenges. *J Biomech*. 2013;46:299-306.
38. Gillis H, Lutchen K. How heterogeneous bronchoconstriction affects ventilation distribution in human lungs: a morphometric model. *Ann Biomed Eng*. 1999;27:14-22.
39. Walker HK, Hall WD, Hurst JW. *Clinical Methods, 3rd edition. The History, Physical, and Laboratory Examinations*. Boston: Butterworth Publishers; 1990.
40. Schurhoff F, Golmard JL, Bellivier F, Berthier A. Admixture analysis of age at onset in schizophrenia. *Schizophrenia Res*. 2004;71:35-41.

How to cite this article: Sanmiguel-Rojas E, Burgos MA, del Pino C, Sevilla-García MA, Esteban-Ortega F. Robust nondimensional estimators to assess the nasal airflow in health and disease. *Int J Numer Meth Biomed Engng*. 2018;34:e2906. https://doi.org/10.1002/cnm.2906